ELSEVIER

Mechanical fatigue of polysilicon: Effects of mean stress and stress amplitude

H. Kahn [a,*], L. Chen [b], R. Ballarini [b], A.H. Heuer [a]

[a] *Department of Materials Science and Engineering, Case Western Reserve University, 10900 Euclid Avenue, Cleveland, OH 44106 7204, USA*
[b] *Department of Civil Engineering, Case Western Reserve University, 10900 Euclid Avenue, Cleveland, OH 44106 7204, USA*

Abstract

Polycrystalline silicon (polysilicon) fatigue specimens with micrometer-sized dimensions were fabricated and subjected to cyclic loading using an integrated electrostatic actuator. The fatigue effects were determined by comparing the single edge-notched beam monotonic bend strength measured after cyclic loading to the monotonic strength of "virgin" specimens that had received no cycling. Both strengthening and weakening were observed, depending on the levels of mean stress and fatigue stress amplitude during the cyclic loading. Monotonic loading with similar sub-critical stress levels had no effect. The physical mechanisms responsible for this behavior are discussed, and a model based on grain boundary plasticity is presented for the strengthening behavior.

© 2005 Published by Elsevier Ltd on behalf of Acta Materialia Inc.

Keywords: Fracture; Fatigue; Semiconductor; Micromechanical modeling

1. Introduction

Polysilicon deposited by low-pressure chemical vapor deposition (LPCVD) is a commonly used material both for integrated circuit applications and for microelectromechanical systems (MEMS). Therefore, its mechanical reliability, including its fatigue resistance, is of great interest. Though polysilicon is a brittle material, dynamic fatigue – delayed fracture under applied cyclic stresses – has been well-documented [1–7]. Fatigue in polysilicon has been reported for both tension/compression stress cycling (load ratio $R = -1$) [2–4] and for zero/tension stress cycling ($R = 0$) [6,7]. (For fatigue cycling, the load ratio, R, is the ratio of the minimum stress to the maximum stress in the cycle. Tension is taken as positive, compression as negative.)

For both cases ($R = -1$ and 0), the lifetime under high-cycle fatigue depends only on the number of cycles, not on the total time or the frequency of the test, for testing frequencies ranging from 1 Hz to 40 kHz [6]. This implies that dynamic fatigue depends only on the applied stresses; we believe it must be mechanical in origin, and not due to time-dependent environmental effects such as stress corrosion, oxidation, or other chemical reactions, although contrary views have been expressed (see below). In fact, we recently showed that low-cycle fatigue strengths are strongly influenced by R, but not by the ambient (air or vacuum) [2]. However, our high-cycle fatigue lives were adversely affected by a humid ambient [2], which was recently corroborated by Alsem et al. [5]. Van Arsdell and Brown [8] also reported that nanoindenter-induced pre-cracks in polysilicon specimens grew when cyclically loaded in humid air (>50% relative humidity), but not in dry air. We postulated that in air, surface oxide formation on mechanically induced subcritical cracks caused wedging effects that increased the applied stress intensity at the subcritical crack tips; on the other hand, Van Arsdell and Brown attributed their results to surface oxidation of the crack tip followed by stress corrosion of the oxide in humid air to extend the crack. (Stress corrosion of SiO_2 in humid air is well documented [9].)

There is another possible explanation for enhanced fatigue in humid ambients that does not involve chemical

---

* Corresponding author. Tel.: +1 216 368 6384.
E-mail address: harold.kahn@case.edu (H. Kahn).

2   *H. Kahn et al. / Acta Materialia xxx (2005) xxx–xxx*

reaction with the environment. Increasing the relative humidity in operating air greatly reduces the amount of wear debris formed by contacting polysilicon components [10]. In fatigue of bulk ceramics, wear debris reduces crack growth by preventing cracks from fully closing [11]. Therefore, similar wear debris formed in dry air or in vacuum could reduce the fatigue effects in polysilicon operated in these ambients.

It has also been reported that the surfaces in the immediate vicinity of fatigue cracks become rougher after cycling — increasing from an R_a (arithmetic average) roughness of 8.9–17.2 nm [6], and from an rms roughness of 10–22 nm [12] – as measured by atomic force microscopy. It is important to note that both of these studies, as well as others [4,5,8], tested polysilicon devices fabricated by the MEMSCAP (formerly JDS Uniphase, Cronos, and MCNC) Multi-User MEMS Processes (MUMPs) program. This process uses P-doped polysilicon that apparently forms extremely thick "native" surface oxides (≈ 30 nm) after release [4], and the increase in rms roughness has been attributed to a stress-assisted nonuniform dissolution of the surface oxide [12]. (These thick surface oxides have been attributed to galvanic effects between the P-doped polysilicon and deposited Au contacts [13].) By contrast, our in-house fabricated undoped polysilicon displays the usual thin (≈ 2 nm thick) native surface oxides after release, as measured by X-ray photoelectron spectroscopy (XPS) depth profiling. We have also shown that polysilicon devices with thermally grown oxides of 45 nm or thicker are susceptible to delayed failure when subjected to monotonic tensile loads in humid air, presumably due to stress corrosion in the surface oxide, while identical devices with thin native oxides (≈ 2 nm thick) do not undergo delayed failure [14].

It is apparent that surface oxides and surface oxidation can affect the behavior of polysilicon devices under cyclic loading, and it has even been suggested that cyclic stressing of polysilicon promotes oxide formation [4,5,12]. However, it is also clear from the absence of a frequency dependence on lifetime [6] and from the equivalence of low-cycle fatigue strength in air and vacuum [2], that mechanical stresses, rather than environmental interactions, are the principal origin of polysilicon fatigue. It is the goal of this paper to systematically explore the effects of applied cyclic stresses on the fatigue behavior. Specifically, we subjected polysilicon specimens to cyclic loading with independently varied mean stresses, σ_m, and fatigue stress amplitudes, $\Delta\sigma$, and subsequently measured the resulting monotonic bend strength.

2. Experiment

The micromachined polysilicon device used in this investigation is shown in Fig. 1. Devices were fabricated from 5.7 μm thick LPCVD polysilicon films, using standard micromachining techniques described previously [3]. The polysilicon films were deposited as multilayers [15], five in the present specimens, and were annealed in nitrogen at 1100 °C for one hour to reduce residual stresses to less than 10 MPa. The resulting microstructures are relatively equiaxed and fine-grained (grain diameters ≈ 100–300 nm); a typical example is shown in Fig. 2. The presence of the nascent interfaces between the five polysilicon layers does not affect the fracture behavior [16].

The electrostatic comb-drive microactuator shown in Fig. 1(a), described previously [3], contains 1438 pairs of interdigitated comb fingers. It allows constant, monotonically increasing, or cyclic loading, depending on whether direct current (DC) or alternating current (AC) voltages are applied. (The resonance frequencies of the devices are approximately 10 kHz.) Cyclic loading with a finite mean stress, σ_m, can be achieved by adding an AC voltage to a DC bias. Figs. 1(b) and (c) show two different single edge-notched beam fracture mechanics specimens that can be integrated with the microactuator. The microactuator can move in only one direction with an applied DC voltage (to the left as shown in Fig. 1(a)), whether the voltage is positive or negative. Therefore, a DC voltage will generate tensile stresses at the notch root in the specimen in Fig. 1(b) and compressive stresses at the notch root in the
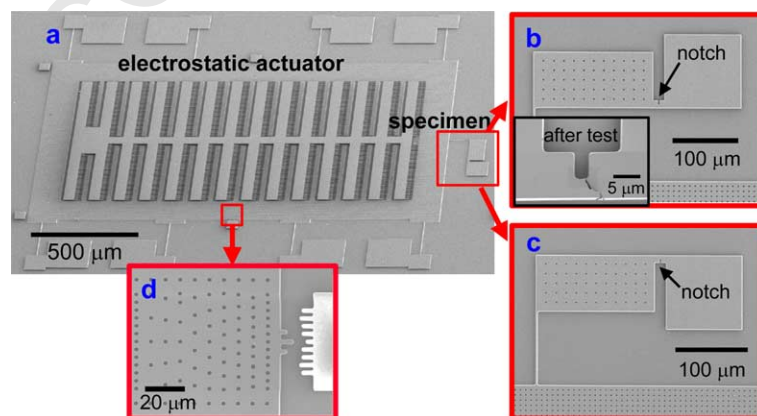

Fig. 1. Scanning electron microscopy (SEM) images of a micromachined device for measuring bend strength and fatigue resistance. (a) The electrostatic actuator integrated with the fracture mechanics specimen. (b,c) Higher magnification rotated images of two single edge-notched fatigue specimens that can be integrated with the actuator; the inset in (b) shows the notch area after testing. (d) Higher magnification rotated image of the measurement scale.
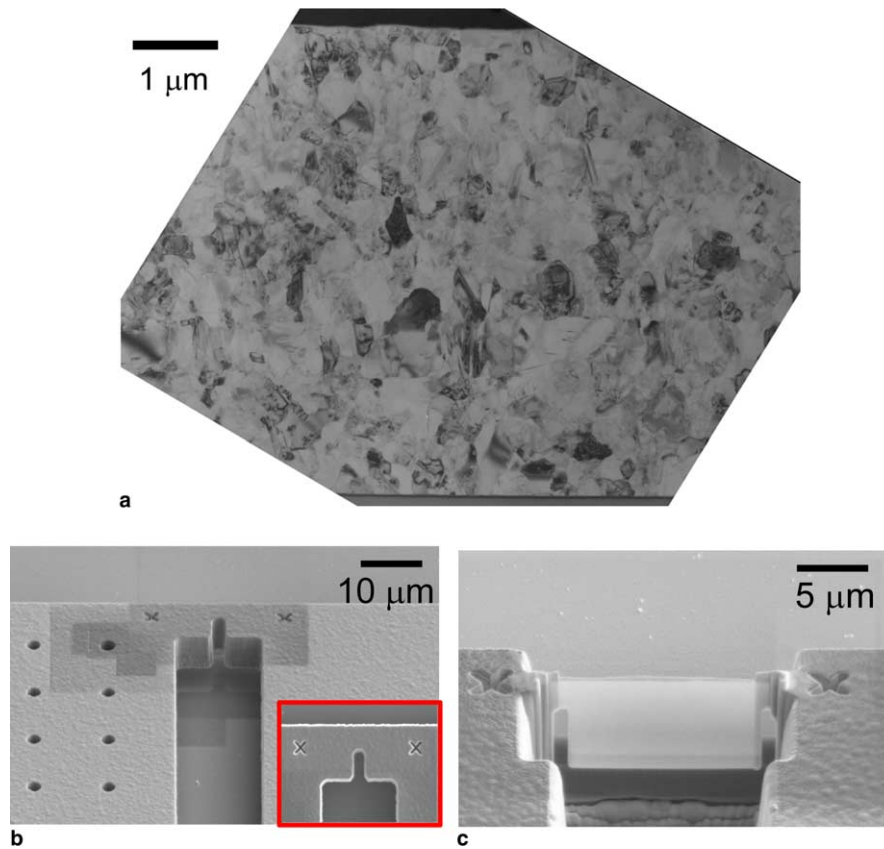
Fig. 2. (a) Cross-sectional transmission electron microscopy (TEM) image of the LPCVD polysilicon film. (b,c) SEM images illustrating how the TEM specimen was cut from a fatigue specimen using a FEI DualBeam 235 focused ion beam (FIB) instrument. (b) The original ×-marks between which a Pt line was deposited to delineate the desired specimen; the inset is a top view. (c) The thin TEM-ready section after FIB milling.

specimen in Fig. 1(c). The different strength and fatigue tests that have been performed are shown schematically in Fig. 3. Fig. 3(a) shows a standard monotonic bend strength, σ_{crit}, test. Fig. 3(b) shows a constant stress hold, σ_{hold}, test, which is followed by a measurement of the monotonic bend strength. Fig. 3(c) shows a ramped $\Delta\sigma$ test. In this test, a DC voltage is first applied to generate a mean stress; then an AC voltage is applied at the resonance frequency, and the amplitude of the AC voltage is increased until catastrophic fracture occurs at the notch root. Typically, the test takes less than 1 minute to complete. The fatigue strength is assumed to be equal to the critical tensile stress required for catastrophic crack propagation, σ_{crit}, and is taken as the maximum tensile stress of the final stress cycle.
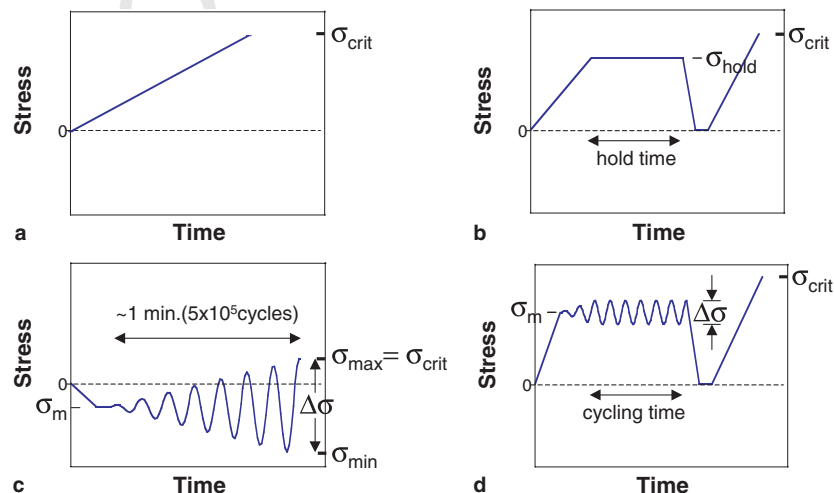

Fig. 3. Schematic representations of the stresses seen at the notches of the specimens shown in Fig. 1, during four types of mechanical strength tests. See text for further details.

One disadvantage of the ramped $\Delta\sigma$ fatigue test (Fig. 3(c)) is that $\Delta\sigma$ and σ_m are not completely independent. For a given σ_m, the $\Delta\sigma$ must be high enough that the maximum stress in the cycle exceeds the fracture strength. Therefore, the effects of small $\Delta\sigma$, particularly for compressive σ_m, cannot be explored in this test. To independently investigate the effects of $\Delta\sigma$ and σ_m, constant $\Delta\sigma$ tests were run, as shown in Fig. 3(d). Here a constant $\Delta\sigma$ is maintained for a fixed time, which is followed by a measurement of the monotonic bend strength. The only tests of this type that cannot be performed are those with highly tensile σ_m and high $\Delta\sigma$, since in this case the maximum stress in the cycle would exceed σ_{crit}.

σ_{hold} in Fig. 3(b) and σ_m in Fig. 3(c) and (d) can be tensile or compressive. When the test requires both tensile and compressive loads (such as Fig. 3(c) when σ_{hold} is compressive), loading in the "opposite" direction is achieved by mechanically displacing the actuator with a micromanipulated probe, as the microactuator can only move in one direction under an applied DC voltage. Obviously, cyclic stresses cannot be achieved using this pushing technique.

For all tests, the deflection of the microactuator was optically monitored throughout the test. Fig. 1(d) shows the region of the microactuator near the measurement scale. Constructive interference of the variably spaced holes in the actuator assists in determining the amplitude of the cyclic deflections. (The holes also facilitate etching of the sacrificial oxide during hydrofluoric acid release.) Finite element analysis (FEA) of the device is used to relate the deflection of the microactuator to the deflection of the fracture mechanics specimen and to the stress at the notch root. For FEA, Young's modulus of polysilicon is assumed to be 164 GPa [17].

Devices were fabricated from undoped polysilicon. The devices could be B-doped, by boron diffusion at the wafer level after polysilicon etching [3]. For the undoped devices, a thin Pd film was sputtered onto the devices, just before testing, to achieve sufficient conductivity for electrostatic actuation, and it was of interest to ascertain if the Pd affects the mechanical behavior. The Pd films were DC sputter-coated using a Denton Vacuum Desk II sputterer at $\approx$50 mTorr (6.7 Pa) Ar, $\approx$45 mA, for 40 s. A scanning electron microscopy (SEM) image of a sputtered Pd film on a (1 0 0) Si wafer is shown in Fig. 4(a). The thickness of this film was measured with a Veeco Instruments Dektak 3030ST profilometer to be 17 ± 3 nm, and the SEM image indicates an uneven morphology. Surface analysis of the film using XPS did not detect Si; this suggests that the Pd film is continuous, although the X-ray incidence angle of 45° may have allowed the higher Pd features to shadow any exposed Si. A transmission electron microscopy (TEM) image of a Pd film deposited onto an amorphous carbon substrate using the same sputtering conditions with a sputtering time of 60 s is shown in Fig. 4(b). As in the SEM image, the TEM images indicate an uneven morphology, and suggest gaps among interconnected Pd islands. However, it should be noted that the presence of very thin Pd regions in the gaps, up to several monolayers thick, would not provide sufficient contrast to be detected by TEM.

The observations in Fig. 4 indicate that the Pd film sputtered onto the polysilicon actuators consists of a network of coalesced islands, which is sufficiently continuous to provide adequate conductivity. It is not clear whether or not any polysilicon is completely exposed, but there are certainly areas of very thin Pd, and the spacing between these areas is approximately equal to the film thickness, 17 nm. It is noted that the films in Fig. 4 were deposited onto very smooth substrates. On the polysilicon devices, the inner surfaces of the notches display roughness due to the plasma etching [16], and therefore the Pd coatings on these surfaces may exhibit more uneven morphologies.

3. Results

Fig. 5(a) shows the single edge-notched beam monotonic strength, σ_{crit}, measurements (Fig. 3(a)) of B-doped polysilicon specimens with and without sputtered Pd. The data
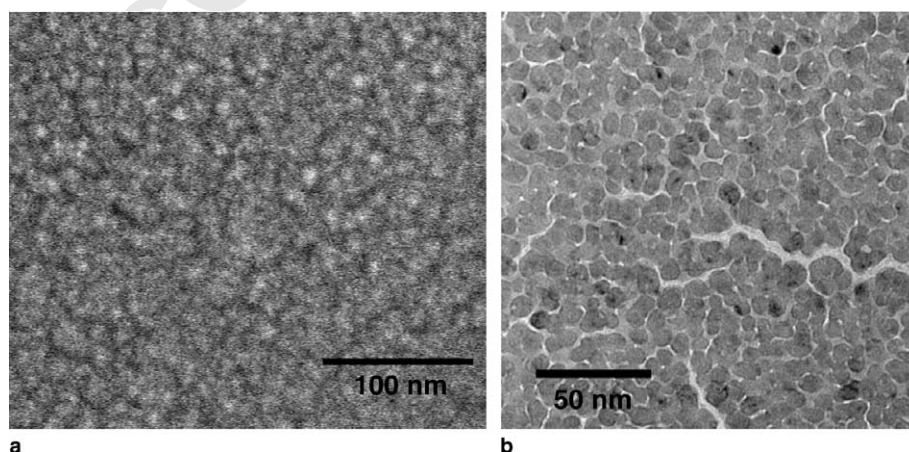

Fig. 4. Images of thin sputtered Pd films. (a) SEM image of a 40 s sputtered Pd film on single crystal (1 0 0) Si; (b) TEM image of a 60 s sputtered Pd film on amorphous carbon.
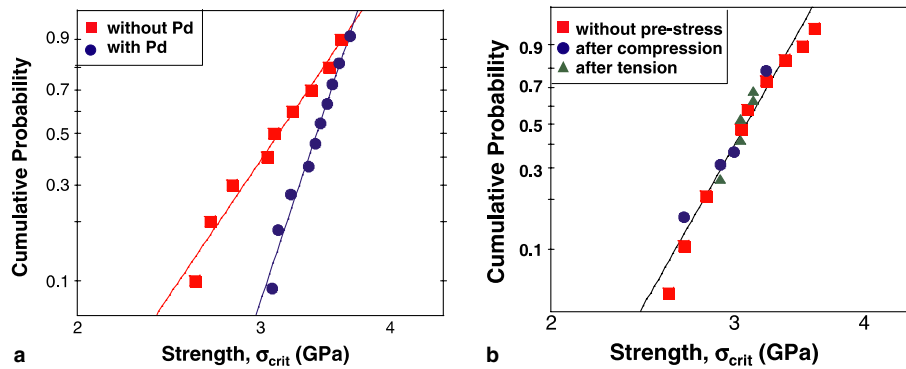
5

Fig. 5. (a) Monotonic strength results for B-doped polysilicon with (circles) and without (squares) sputtered Pd. The data display averages and Weibull moduli of 3.4 GPa and 17 for samples with Pd and 3.1 GPa and 8.5 for samples without Pd. (b) Monotonic B-doped polysilicon bend test results, including data from standard bend tests (squares, Fig. 3(a)) and data from tests of samples that endured a constant hold stress before monotonic strength testing (Fig. 3(b)). A single Weibull distribution describes all the data; the average strength is 3.1 GPa, and the Weibull modulus is 12.

225 are shown in a Weibull probability plot, with the straight-
226 line fits indicating the expected adherence to Weibull statis-
227 tics for brittle fracture. The addition of Pd increases the
228 average bend strength by about 10%. Since fracture of
229 the specimens originates on the inner surfaces of the
230 notches [3,16], the Pd on these surfaces must produce a
231 modicum of strengthening, possibly by diminishing the
232 severity of the "Griffith flaws" that cause catastrophic fail-
233 ure. (The uncertainty of each bend strength measurement is
234 about ±0.15 GPa, which arises from an uncertainty in
235 actuator deflection of about ±0.3 μm.)
236   To determine whether highly compressive or tensile
237 monotonic stresses can affect the monotonic strength, con-
238 stant σ_{hold} tests (Fig. 3(b)) were performed. These results are
239 compared with standard monotonic σ_{crit} tests (Fig. 3(a)) in
240 a Weibull probability plot in Fig. 5(b), and include data
241 from standard bend tests (squares), data from samples that
242 endured a constant compressive hold stress before mono-
243 tonic strength testing (circles, $\sigma_{hold} = -4.5$ GPa for a few
244 seconds), and data from samples that endured a constant
245 tensile hold stress before monotonic strength testing (trian-
246 gles, $\sigma_{hold} = 2.7$ GPa for about 10 min). For both cases –
247 compressive σ_{hold} and tensile σ_{hold} – there are no significant
248 differences in the observed σ_{crit}.

249   Fig. 6 shows results from ramped $\Delta\sigma$ fatigue tests
250 (Fig. 3(c)) of undoped (with sputtered Pd) and B-doped
251 (without Pd) polysilicon, plotted as fatigue strength versus
252 σ_m. (We reported the data in Fig. 6(a) in a previous paper
253 [2] as fatigue strength versus R.) The undoped results
254 include data taken in air (10^5 Pa) and vacuum (10 Pa).
255 The behavior in the two ambients is indistinguishable.
256 Also, the dependence of fatigue strength on σ_m is similar
257 for both doped and undoped specimens – varying σ_m from
258 highly tensile to highly compressive leads to a marked
259 decrease in fatigue strength. We previously showed fracto-
260 graphs for specimens tested with both highly tensile and
261 highly compressive σ_m [2]. The "mirror" region on the frac-
262 ture surface of the compressively biased specimen was sig-
263 nificantly larger than that on the specimen that had
264 experienced a tensile bias, indicating that sub-critical crack
265 growth occurred during the cyclic stressing of the compres-
266 sively biased specimen.
267   In Fig. 6(a) and (b), the monotonic bend strengths, σ_{crit},
268 taken from specimens that had experienced no cycling, are
269 also presented. It is clear that a compressive σ_m leads to a
270 significant decrease in σ_{crit}. Both plots, particularly
271 Fig. 6(a), also suggest that a highly tensile σ_m leads to an
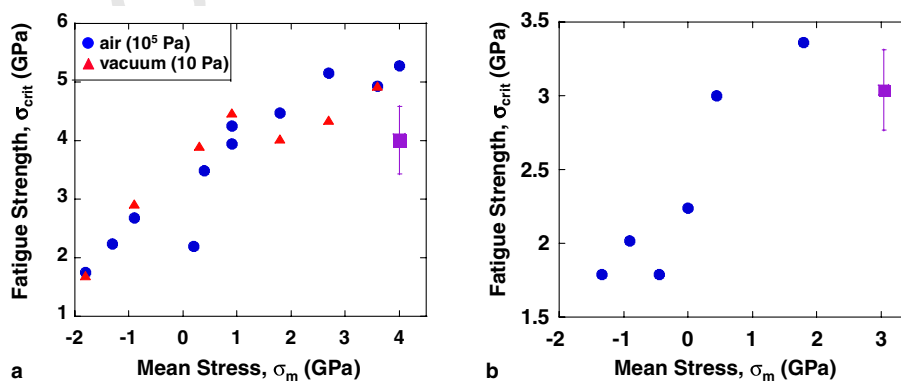272 increase in σ_{crit} for these ramped $\Delta\sigma$ fatigue tests. Since

Fig. 6. Results from increasing $\Delta\sigma$ fatigue tests (Fig. 3(c)) of polysilicon in air (circles) and vacuum (triangles). (a) Data for Pd-coated undoped polysilicon, and (b) data from B-doped polysilicon with no Pd. In each plot the monotonic strength, taken from specimens that saw no cycling, is shown as the solid square; the square marks the average strength, and the error bars represent one standard deviation.

the results in Fig. 5(b) rule out any effects due simply to monotonic stresses, the trends shown in Fig. 6 must be caused by cyclic stresses.

Fig. 7(a) shows results for constant $\Delta\sigma$ tests (Fig. 3(d)) where σ_m was fixed at -2.2 GPa, and $\Delta\sigma$ was varied. The cycling time was 10 min, equivalent to $\approx 6 \times 10^6$ cycles. For this σ_m, cycling with small $\Delta\sigma$ does not affect the σ_{crit} measured after cyclic stressing, but cycling with large $\Delta\sigma$ leads to a decrease in σ_{crit}. This implies that the weakening seen for compressive σ_m in Fig. 6 is due to the large $\Delta\sigma$ experienced by these specimens, and not solely because of the compressive σ_m.

Fig. 7(b) Shows the results for constant $\Delta\sigma$ tests of undoped polysilicon where $\Delta\sigma$ was fixed at 2.0 GPa (± 1.0 GPa), and σ_m was varied. The cycling time was 10 min, equivalent to ≈ 5–8×10^6 cycles (for higher absolute values of σ_m, the resonant frequency of the device increases). For small tensile or compressive σ_m, σ_{crit} is unaffected by the relatively small $\Delta\sigma$ cycling. However, for large tensile or compressive σ_m, σ_{crit} is enhanced. In the experiments with the highest tensile σ_m, 2.0 GPa, the maximum tensile stress seen at the notch root during cycling was 3.0 GPa. This exceeds the average monotonic bend strength, 2.7 GPa, though it falls within one standard deviation, 0.4 GPa. As shown in Fig. 3(d), once the σ_m is applied, the cyclic stresses are ramped up to the desired $\Delta\sigma$. None of the five specimens tested under these condi-

tions broke when the cyclic stresses were ramped up to a σ_{max} of 3.0 GPa. Statistically, it is highly unlikely that all five specimens would have displayed σ_{crit} greater than 3.0 GPa without any cycling. Therefore, it is presumed that during the ramp up of the cyclic stress, which takes several seconds ($\approx 10^5$ cycles), enough strengthening occurred in the specimens to survive a σ_{max} of 3.0 GPa.

Fig. 7(c) Shows results for similar constant $\Delta\sigma$ tests of B-doped polysilicon (no Pd). For σ_m of 1.8 GPa, $\Delta\sigma$ was 1.8 GPa, and for σ_m of 2.2 GPa, $\Delta\sigma$ was 0.9 GPa. The cycling time was 10 min, equivalent to ≈ 6–7×10^6 cycles. As with the undoped specimens, low amplitude cycling with high σ_m leads to apparent strengthening. The effect is not as apparent as for the undoped specimens, but the maximum σ_m in these tests is a slightly smaller fraction of σ_{crit} than in the undoped polysilicon tests. Student's t tests were performed comparing the two sets of constant $\Delta\sigma$ data in Fig. 7(c) with the 18 results used to produce the average monotonic bend strength shown in the plot. For $\sigma_m = 1.8$ GPa, the change in σ_{crit} is not significant ($0.10 > P > 0.05$), but for $\sigma_m = 2.2$ GPa, the increase in σ_{crit} is significant ($0.05 > P > 0.01$). This result indicates that the sputtered Pd film is not responsible for the strengthening seen in the undoped polysilicon specimens.

Fig. 8 presents the combined results for all constant $\Delta\sigma$ tests plotted as the measured monotonic bend strength, σ_{crit}, versus the four parameters of cyclic loading, σ_{min},
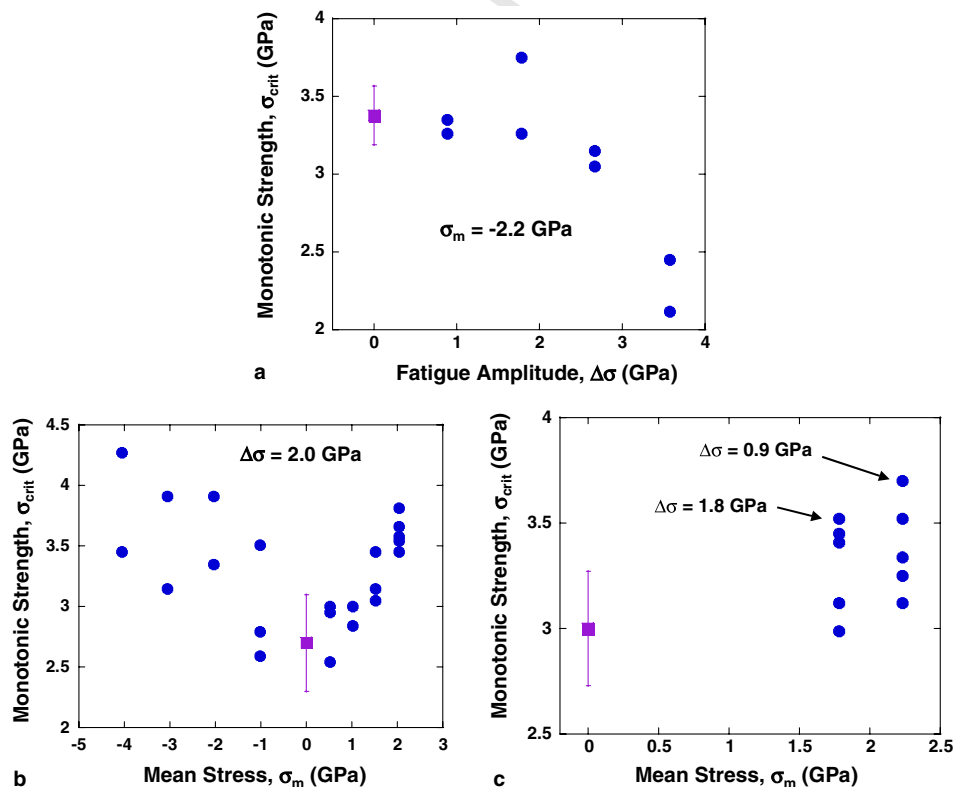

Fig. 7. Results from constant $\Delta\sigma$ fatigue tests (Fig. 3(d)). The monotonic strength, taken from specimens that saw no cycling, is shown as the solid square; the square marks the average strength, and the error bars represent one standard deviation. (a) Data for Pd-coated B-doped polysilicon, where σ_m was -2.2 GPa for all tests. In (b) and (c), $\Delta\sigma$ was fixed. In (b), $\Delta\sigma$ was 2.0 GPa for all tests, and the samples were Pd-coated undoped polysilicon. In (c) the samples were B-doped polysilicon with no Pd. $\Delta\sigma$ was 1.8 GPa for the tests with σ_m of 1.8 GPa, and 0.9 GPa for the tests with σ_m of 2.2 GPa.
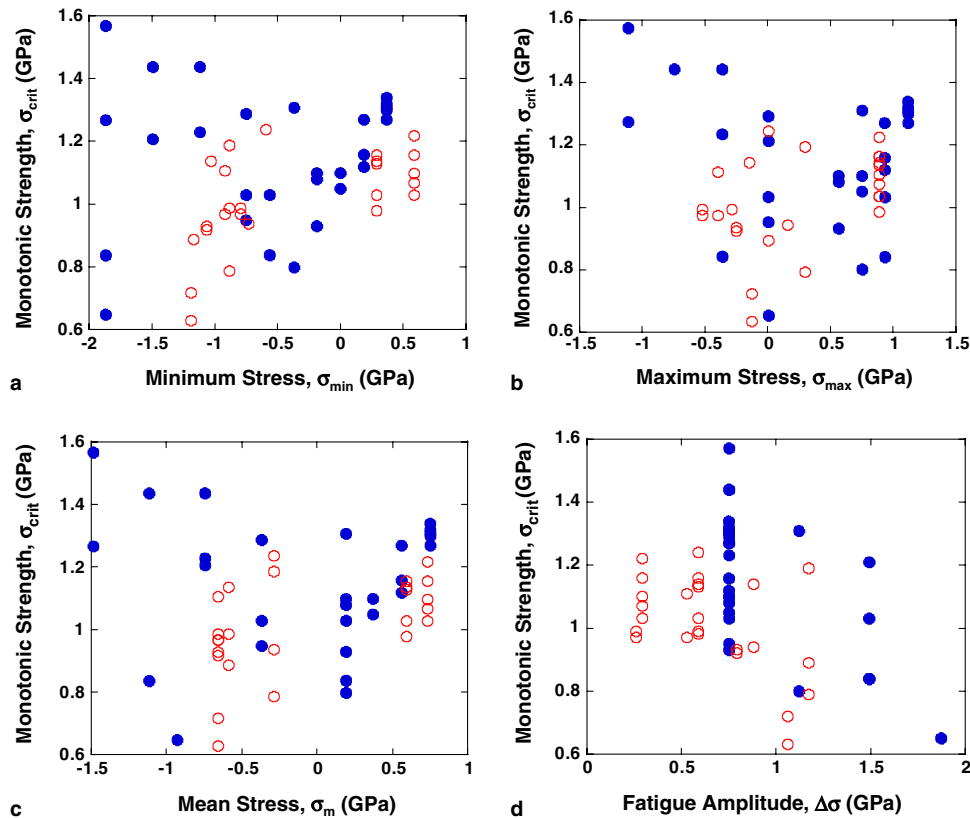
Fig. 8. Results from constant $\Delta\sigma$ fatigue tests (Fig. 3(d)) of undoped (filled symbols) and B-doped (open symbols) polysilicon. The measured monotonic strengths after cycling and the stress levels are normalized by dividing by the average monotonic strength determined with no cycling.

σ_{max}, σ_m, and $\Delta\sigma$. Since the wafers had slightly different average strengths due to stochastic differences in processing affecting the severity of "Griffith" flaws, the measured strengths and the loading parameters are normalized by dividing by the average monotonic strength (as determined by specimens that saw no cycling). It is clear that σ_{crit} is not directly dependent on any individual parameter. However, a three-dimensional plot of the normalized σ_{crit} versus σ_m and $\Delta\sigma$ (Fig. 9(a)) reveals that, while there is significant scatter in the data typical of brittle fracture phenomena, qualitative trends exist when these two parameters are combined. These trends are summarized in Fig. 9(b).

4. Discussion

Fatigue behavior of polysilicon, determined by measuring the monotonic bend strength after a period of cyclic loading, is strongly influenced by the cyclic stress levels. As seen in Fig. 9, both strengthening and weakening occur in different regimes of $\Delta\sigma$ and σ_m. We presume that the same physical processes control both regimes, and discuss three possible mechanisms to explain the observed behavior: microcracking, dislocation activity, and grain boundary plasticity. Weakening can be produced by microcracking simply by increasing the length of initial flaws. As discussed above, fractography has revealed that the weakened specimens do contain longer initial pre-cracks. Microcracking

in brittle ceramics has been observed after compressive fatigue cycles [18], and after Hertzian contact [19]. Also, debris particles have been observed in the crack wake of fatigued Al_2O_3, which is interpreted as indicating a microcracked crack tip damage zone [20]. On the other hand, to produce strengthening, shallow microcracks must form with close enough spacings to shield the crack tips [21,22]. For example, for the data shown in Fig. 9(a), the average monotonic bend strength without cycling is 2.7 GPa. Given the fracture toughness, K_{Ic}, of polysilicon of 1.0 MPa m$^{1/2}$ [16], this corresponds to an initial pre-crack of 90 nm, using the standard relation

$$K_{Ic} = k\sigma_{crit}(\pi a)^{1/2}, \qquad (1)$$

where σ_{crit} is the stress at failure, a is the size of the crack-initiating flaw, and k is a constant equal to 0.71 for a semi-circular flaw [23]. For closely spaced parallel cracks, the stress intensity, K, at the crack tip can be approximated by replacing the crack size, a, in Eq. (1) with the spacing between the cracks [22]. Therefore, to achieve the $\approx50\%$ increase in monotonic strength seen in Fig. 7(b), the spacing between parallel microcracks must be ≈40 nm. This spacing is smaller than the typical grain diameter of the polysilicon (Fig. 2(a)) by about a factor of five. Therefore, the majority of these microcracks would have to lie within the interior of grains. Though silicon grains undoubtedly contain cleavage planes, it is difficult
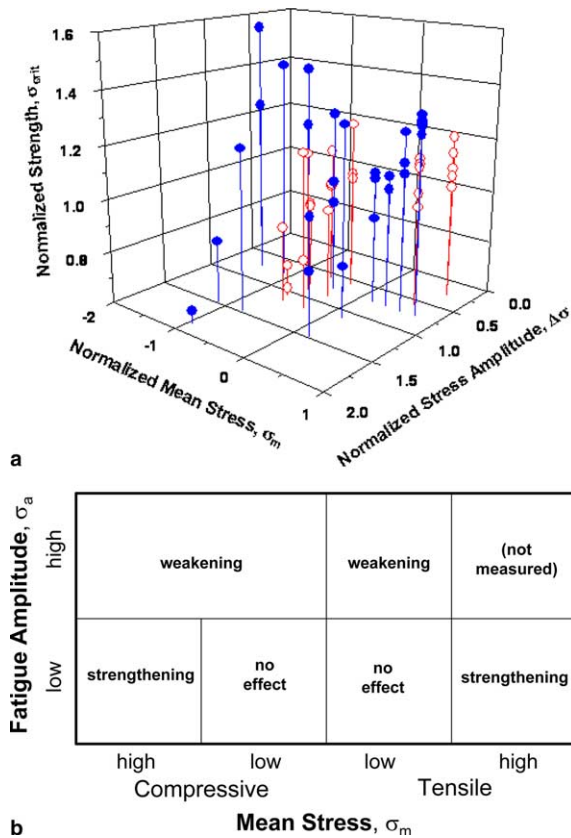
Fig. 9. (a) The normalized results from constant $\Delta\sigma$ fatigue tests of undoped (filled symbols) and B-doped (open symbols) polysilicon. (b) The qualitative effects of $\Delta\sigma$ and σ_m on σ_{crit}.

380 to envision the possible stress conditions that would lead
381 to such a high density of parallel microcracks; lengthening
382 of existing flaws seems much more likely. Therefore, while
383 both weakening and strengthening could conceivably be
384 explained via microcracking phenomena, the strengthen-
385 ing case is less intuitive and frankly unappealing.
386   The second possible mechanism is dislocation activity.
387 Fatigue in metals is generally understood to occur through
388 the plastic blunting of crack tips via irreversible shear and
389 dislocation emission on two slip systems at roughly 45° to
390 the crack plane; subsequent resharpening and crack
391 advance proceeds by continued slip on these two systems
392 [24]. Dislocation activity of this kind could easily explain
393 the strengthening (crack tip blunting) and weakening
394 (crack blunting and resharpening) behavior seen in these
395 polysilicon experiments. However, this mechanism has
396 not been observed in fatigue testing of brittle ceramics at
397 room temperature, though dislocations have been observed
398 in silicon beneath room temperature indents [25,26] and in
399 high-pressure anvil experiments [27], along with evidence of
400 compression-induced phase transformation [28]. Similarly,
401 dislocations have been generated in silicon beneath tung-
402 sten studs by room temperature ultrasonic cleaning [29].
403 In both of these cases, the mechanical constraints of the sil-
404 icon substrate coupled with the applied shear stresses are
405 thought to have caused dislocation nucleation and motion.

406 This latter situation is analogous to the small $\Delta\sigma$ cycling
407 with high compressive σ_m (the left side of Fig. 7(b)). The
408 compressive stresses supply both the mechanical constraint
409 and the shear stress. The same level of shear stress will be
410 generated with a high tensile σ_m (the right side of
411 Fig. 7(b)). However, in this case, the mechanical constraint
412 is not present, and the applied shear (and bending) stresses
413 would be expected to cause crack extension and brittle frac-
414 ture instead of dislocation emission [30]. For similar rea-
415 sons, TEM investigations of cracks in silicon have
416 generally not detected dislocations at arrested crack tips
417 [31–33].
418   It is also possible that internal friction effects generate
419 localized heating in the area around the notch root in the
420 polysilicon specimen during resonance testing, which
421 would further promote dislocation activity. Though Muhl-
422 stein et al. [4] reported that infrared imaging of a similar
423 device did not reveal any temperature increase at the notch
424 root, their spatial resolution of 8 μm may have been too
425 coarse to detect very local effects. To investigate heating,
426 we sputtered a thin (≈20 nm) Au film onto a polysilicon
427 device and subjected it to the same cyclic loading condi-
428 tions that caused strengthening in Fig. 7(b). After cycling,
429 no morphological changes in the Au film at the notch root
430 could be observed in the SEM, suggesting that the Au–Si
431 eutectic temperature of 363 °C had not been reached. Since
432 the brittle–ductile transition temperature of silicon is at
433 least 700 °C, and increases with increasing strain rates
434 [34], polysilicon is expected to behave as a brittle material
435 in these experiments.
436   The final possible explanation is grain boundary plastic-
437 ity. At the polysilicon grain boundaries, there could well be
438 a thin region of "amorphous" silicon that is susceptible to
439 a non-conventional form of plastic deformation in shear
440 [35]. Even in the absence of an amorphous material, the
441 bonding at the grain boundaries will be imperfect com-
442 pared to the bulk and could be susceptible to shear defor-
443 mation. This grain boundary plasticity could produce local
444 residual stresses that will depend on the local microstruc-
445 ture and which will affect apparent strengths. This model
446 is discussed with respect to the strengthening behavior in
447 the next section.

4.1. Plastic flow in amorphous silicon and the Drucker–Prager model

450   A possible explanation for the strengthening is that the
451 cyclic loading leads to some sort of plastic deformation
452 near the root of the notch, which gives rise to residual com-
453 pressive stresses upon unloading. The compressive pre-
454 stress would result in a higher apparent strength when
455 the structure is subsequently loaded in monotonically
456 increasing tension. This possibility is supported by the
457 molecular dynamics calculations performed by Demkowicz
458 and Argon [35], which show that amorphous silicon can
459 undergo a non-traditional form of plastic deformation. If
460 the polysilicon grain boundaries can be considered a thin

region of amorphous silicon, then under certain levels of mean stress and stress amplitude, plasticity could have evolved along the grain boundaries, and compressive residual stresses could have developed at the root of the notch upon removal of the loads.

The molecular dynamics simulations involved shear loading at constant volume. Using the Stillinger–Weber empirical potential for silicon [36], Demkowicz and Argon created amorphous samples with four different initial densities by "melting" the diamond cubic crystal structure, and then slowly quenching the liquid at different rates using constant pressure molecular dynamics. For four values of initial density, ρ, the calculated deviatoric stress and pressure as functions of deviatoric strain are shown in Fig. 10. The plasticity is very sensitive to the density of the initial unstressed amorphous silicon, and can produce either dilatancy or compaction (the pressure in the constant volume simulations increases or decreases). For the lowest density simulation, elastic loading terminated with a sharp yield phenomenon that was followed by significant strain softening and concomitant large drop in system pressure. As pointed out by Demkowicz and Argon, the pressure drop, which implies compaction in a constant pressure simulation, is opposite to the behavior of metallic glasses, which expand during deformation. For the two higher densities, the plastic deformation is associated with an increase in pressure, implying that under constant pressure the silicon would dilate. The plastic deformation predicted by the atomistic calculations can be approximated using the Drucker–Prager [37] plasticity model that has been applied to geo-materials (such as rock, concrete, and soil) whose shear strength depends on pressure and whose plastic deformation involves dilatation. The yield surface (function), schematically shown in Fig. 10(c), is defined as

$$F = \sigma_e - p \tan \beta - c = 0, \qquad (2)$$

where $\sigma_e = \sqrt{\frac{3}{2} s_{ij} s_{ij}}$ is the equivalent (von Mises) stress, β is the friction angle, and $c = \sqrt{3}\tau_0$ is the cohesion of the material written in terms of the shear strength τ_0. β determines the sensitivity of the shear strength to the pressure.

The plastic (flow) potential is

$$G = \sigma_e - p \tan \psi, \qquad (3)$$

where ψ is the dilatation angle, which controls the level of unit volume change. The increments of plastic strain are obtained from the potential as

$$d\varepsilon_{ij}^{p} = d\lambda \frac{\partial G}{\partial \sigma_{ij}}, \qquad (4)$$

where

$$d\lambda = \frac{d\varepsilon^{p}}{1 - \frac{1}{3} \tan \psi} \qquad (5)$$

and $d\varepsilon^{p} = \sqrt{\frac{2}{3} d\varepsilon_{ij}^{p} d\varepsilon_{ij}^{p}}$ is the equivalent plastic strain increment.

The deviatoric stresses and pressures (Fig. 10) as functions of deviatoric strain [35] were used as inputs into the
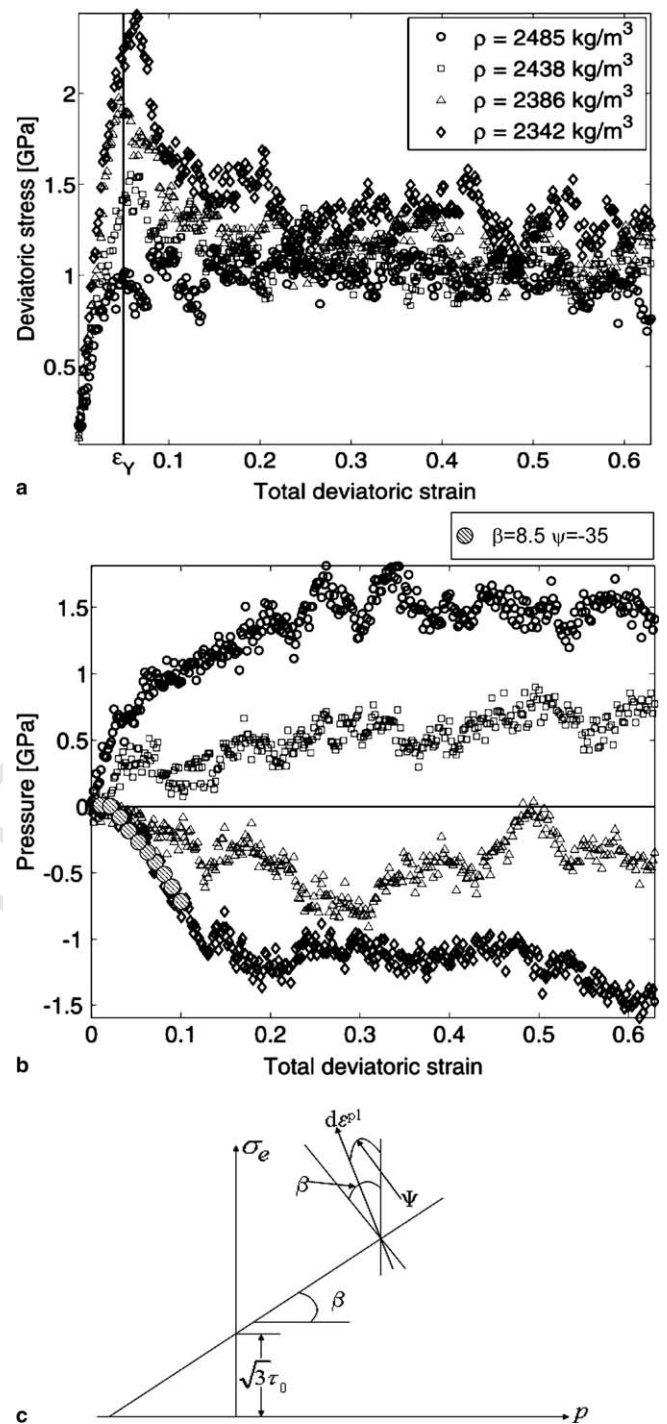

Fig. 10. (a,b) Plastic-like behavior of amorphous silicon predicted by atomistic calculations [34]: (a) deviatoric stress versus deviatoric strain; (b) pressure versus deviatoric strain (the large circles are from our finite element calibration model, using $\beta = 8.5°$ and $\psi = -35°$). (c) Yield surface of linear Drucker–Prager plasticity model.

finite element program ABAQUS [38] to calibrate values of friction angle β, dilatation angle ψ, and relevant isotropic hardening parameters, using a two-dimensional plate, comprised of four-noded quadrilateral elements, subjected to a shear deformation. The elastic modulus of the amorphous silicon was obtained as 150 GPa [35], and Poisson's

ratio was assumed to be 0.22. For initial density $\rho = 2342 \, kg/m^3$, the deviatoric stress–strain response shown in Fig. 10(a) was used as input into the finite element calibration model. The best fit to the pressure–deviatoric strain response were provided by the combination $\beta = 8.5°$, $\psi = -35°$, as shown in Fig. 10(b). Because the friction and dilatation angles are not equal, the plasticity model is nonassociated, and the material stiffness matrices are not symmetric.

As explained subsequently, strengthening is predicted by both dilating and contracting amorphous grain boundaries. The demonstrative simulations to be presented next were performed using the Drucker–Prager parameters corresponding to a relatively low density amorphous silicon, which would compact when deformed.

The plasticity model was used to simulate cyclic loading experiments on the notched specimen shown in Fig. 1. This geometry is representative of the experimental specimens. The stresses near the root of the notch are controlled by the applied traction, σ. Two finite element models were used. The first, shown in Fig. 11, is a local–global model that retains a discrete description of the crystalline structure surrounding the notch, while efficiently incorporating the far-field behavior through a homogenized polysilicon with a Young's modulus equal to 160 GPa and a Poisson's ratio equal to 0.22. The randomly sized crystals, generated through Poisson–Voronoi tessellation [39], have linear dimensions in the range 200–300 nm, and are separated by 1 nm thick grain boundaries made of amorphous silicon. It is noted that the finite element model does not include the three-dimensional geometry of the fine grained polysilicon. Instead, it is a demonstrative plane stress model with columnar grains.

With respect to the loading described in Fig. 3(d), the failure map shown in Fig. 9(b) is explored by applying 500 cycles to each of four combinations of mean stress and stress amplitude: (i) $\sigma_m = 0.8 \, GPa$, $\Delta\sigma = 1.6 \, GPa$ (small tensile mean stress, small stress amplitude), (ii) $\sigma_m = -1.0 \, GPa$, $\Delta\sigma = 1.6 \, GPa$ (small compressive mean stress, small stress amplitude), (iii) $\sigma_m = 2.0 \, GPa$, $\Delta\sigma = 2.0 \, GPa$ (large tensile mean stress, small stress amplitude), (iv) $\sigma_m = -3.5 \, GPa$, $\Delta\sigma = 2.0 \, GPa$ (large compressive mean stress, small stress amplitude).

In agreement with the experimental results, the structure remained elastic for cases (i) and (ii); no residual stresses developed upon removal of the cyclic loading. Therefore no strengthening would be observed upon subsequent tensile loading.

Figs. 11(b) and (c) show the distributions of the stress component σ_{22} near the root of the notch for cases (iii) and (iv). It was observed that after 500 cycles, modest levels of compressive stresses develop; $\sim$0.5–1 GPa for the tensile mean stress and $\sim$0.1–0.3 GPa for the compressive mean stress. However, it was also observed during the finite element simulations that the rate of compressive stress increase was actually higher for the compressive mean stress (case (iv)) toward the end of the 500 cycles.
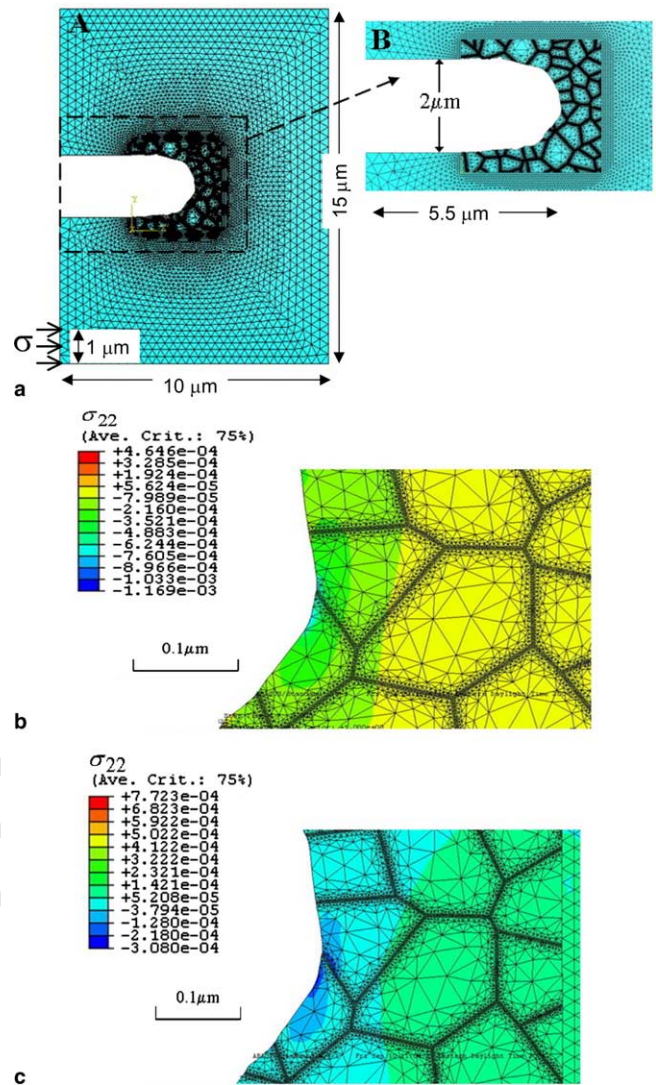

Fig. 11. (a) Local–global model of a notched polysilicon MEMS specimen. The inset is a close-up view of the root of the notch, showing the discrete polycrystalline structure surrounded by homogeneous silicon. (b,c) Residual stress distributions after 500 cycles: (b) $\sigma_m = 2.0 \, GPa$, $\Delta\sigma = 2.0 \, GPa$, (c) $\sigma_m = -3.5 \, GPa$, $\Delta\sigma = 2.0 \, GPa$.

The detailed crystalline description precludes the possibility of simulating a larger number of load cycles in the nonlinear material structural model. Therefore, taking advantage of the fact that the local–global simulations indicated that plastic deformation develops in only one grain boundary, as seen in Fig. 11(b) and (c), the model shown in Fig. 12 was constructed to simulate larger numbers of cycles. This model, involving one grain boundary 216 nm long near the root of the notch, was loaded for 1000 cycles with the aforementioned combinations of mean stress and stress amplitude.

As for the local–global model, no residual stresses develop for the first two cases. Fig. 12 shows the results for $\sigma_m = 2.0 \, GPa$, $\Delta\sigma = 2.0 \, GPa$ and $\sigma_m = -3.5 \, GPa$, $\Delta\sigma = 2.0 \, GPa$. Both cases produce significant residual compressive stresses; $\approx$1.4 GPa maximum compression for the case of tensile mean stress, and $\approx$0.9 GPa maximum

σ_{22}
(Ave. Crit.: 75%)

0.1μm
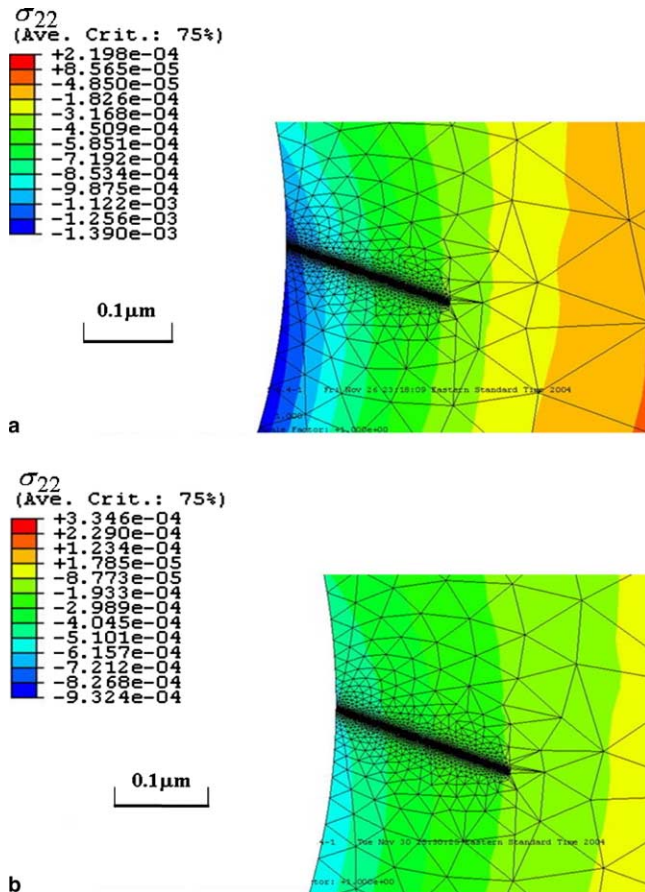
a

σ_{22}
(Ave. Crit.: 75%)

0.1μm

b

Fig. 12. Residual stress distribution in notched polysilicon MEMS specimen after 1000 cycles: (a) $\sigma_m = 2.0$ GPa, $\Delta\sigma = 2.0$ GPa, (b) $\sigma_m = -3.5$ GPa, $\Delta\sigma = 2.0$ GPa.

compression for the case of compressive mean stress. Remarkably, the levels of compressive stress are of the same order as the experimentally observed strengthening.

To determine whether the predictions are sensitive to the dilatant/compactive nature of the plastic deformation, the simulations were repeated with all parameters kept the same except for the dilatancy angle, which was assumed as $\psi = +35°$ (the sign was switched to produce dilatancy). The finite element simulations revealed that the residual stress distribution was very similar to that predicted by the previous model, the largest value of residual compressive stress being slightly higher (≈ 1.43 GPa, compared to ≈ 1.39 GPa). The insensitivity to the sign of the volume change results from the fact that the deviatoric strains remained less than 0.1 for the values of stress applied during the experiments and simulations. As shown in Fig. 10, the dilatation in this range is insignificant. What is important is that sufficiently high levels of plastic deformation occur. Therefore, the level of strengthening is not expected to be sensitive to the assumed grain boundary thickness.

5. Conclusions

Polysilicon displays fatigue behavior. Cyclic loading affects the polysilicon specimens in such a way that the monotonic bend strength is altered; these effects do not occur for sub-critical monotonic loading at similar stress levels. Fatigue stressing can generate both weakening and strengthening, depending on the applied stress levels. A relatively small $\Delta\sigma$ combined with a high σ_m (tensile or compressive) leads to strengthening, while a relatively large $\Delta\sigma$ results in weakening. We present a model that predicts levels of cyclic loading-induced strengthening of polysilicon MEMS structures that are qualitatively and quantitatively consistent with experimental data. The apparent strengthening results from the residual compressive stresses that result from the plastic deformation of amorphous grain boundaries.

References

[1] Kahn H, Ballarini R, Heuer AH. Curr Opin Solid State Mater Sci 2004;8:71.
[2] Kahn H, Ballarini R, Bellante JJ, Heuer AH. Science 2002;298:1215.
[3] Kahn H, Ballarini R, Mullen RL, Heuer AH. Proc R Soc Lond A 1999;455:3807.
[4] Muhlstein CL, Stach EA, Ritchie RO. Acta Mater 2002;50:3579.
[5] Alsem DH, Stach EA, Muhlstein CL, Ritchie RO. Appl Phys Lett 2005;86:041914.
[6] Bagdahn J, Sharpe Jr WN. Sens Actuat A 2003;103:9.
[7] Kapels H, Aigner R, Binder J. IEEE Trans Elec Dev 2000;47:1522.
[8] Van Arsdell WW, Brown SB. J Microelectromech Syst 1999;8:319.
[9] Michalske TA, Freiman SW. J Am Ceram Soc 1983;66:284.
[10] Tanner DM, Walraven JA, Irwin LW, Dugger MT, Smith NF, Eaton WP, et al. IEEE Int Reliab Phys Symp Proc 1999;37:189.
[11] Ewart L, Suresh S. J Mater Sci 1987;22:1173.
[12] Allameh SM, Shrotriya P, Butterwick A, Brown SB, Soboyejo WO. J Microelectromech Syst 2003;12:313.
[13] Kahn H, Deeb C, Chasiotis I, Heuer AH. J Microelectromech Syst [in press].
[14] Kahn H, Ballarini R, Heuer AH. Mater Res Soc Symp Proc 2003;741: J3.4.1.
[15] Yang J, Kahn H, He AQ, Phillips SM, Heuer AH. J Microelectromech Syst 2000;9:485.
[16] Ballarini R, Kahn H, Tayebi N, Heuer AH. Effects of microstructure on the strength and fracture toughness of polysilicon: a wafer level testing approach. In: Muhlstein CL, Brown SN, editors. Mechanical properties of structural films, ASTM STP 1413. West Conshohocken (PA): ASTM; 2001. p. 37.
[17] Jensen BD, de Boer MP, Masters ND, Bitsie F, LaVan DA. J Microelectromech Syst 2001;10:336.
[18] Suresh S. Int J Fract 1990;42:456.
[19] Lawn BR, Padture NP, Guiberteau F, Cai H. Acta Metall Mater 1994;42:1683.
[20] Roebben G, Steen M, Bressers J, Van der Biest O. Prog Mater Sci 1996;40:265.
[21] Hutchinson JW. Acta Metall 1987;35:1605.
[22] Kessler H, Ballarini R, Mullen RL, Kuhn LT, Heuer AH. Comput Mater Sci 1996;5:157.
[23] Newman Jr JC, Raju IS. Eng Fract Mech 1979;11:817.

678 [24] Ritchie RO. Int J Fract 1999;100:55.
679 [25] Lloyd SJ, Molina-Aldareguia JM, Clegg WJ. J Mater Res 2001;16:
680 3347.
681 [26] Hill MJ, Rowcliffe DJ. J Mater Sci 1974;9:1569.
682 [27] Rabier J, Denanot MF, Demenet JL, Cordier P. Mater Sci Eng A
683 2004;387–389:124.
684 [28] Ge D, Domnich V, Gogotsi Y. J Appl Phys 2003;93:2418.
685 [29] Kato NI, Nishikawa A, Saka H. Mater Sci Semicond Proc 2001;4:
686 113.
687 [30] Rice JR, Beltz GE. J Mech Phys Sol 1994;42:333.

688 [31] Lawn BR, Hockey BJ, Wiederhorn SM. J Mater Sci 1980;15:1207.
689 [32] Tanaka H, Bando Y. J Am Ceram Soc 1990;73:761.
690 [33] Wu YQ, Xu YB. Philos Mag Lett 1998;78:9.
691 [34] St. John C. Philos Mag 1975;32:1193.
692 [35] Demkowicz MJ, Argon AS. Phys Rev Lett 2004;93:025505.
693 [36] Stillinger FH, Weber TA. Phys Rev B 1988;37:4132.
694 [37] Chen WF. Plasticity in reinforced concrete. New York (NY): Mc-
695 Graw-Hill; 1982.
696 [38] ABAQUS, Hibbitt, Karlsson & Sorensen, Inc., Pawtucket, RI.
697 [39] Mullen RL, Ballarini R, Yin Y. Acta Metall Mater 1997;45:2247.
698